

Article

Study on Force Characteristics and Safety of Segment Structure and Bolts with and without Cavity behind Lining with Multi-Field Coupling

Feilong Li ^{1,2,3}, Changshan Jiang ^{2,3}, Guoqing Cai ¹, Jianjun Luo ^{1,*}, Qian Yu ^{2,3}, Heqing Zhang ^{2,3} and Lei Wang ^{1,4}

¹ School of Civil Engineering, Beijing Jiaotong University, Beijing 100044, China; 18115026@bjtu.edu.cn (F.L.); guoqing.cai@bjtu.edu.cn (G.C.); 17115298@bjtu.edu.cn (L.W.)

² China Airport Planning & Design Institute Co., Ltd., Beijing 101312, China; csjiangcacc@126.com (C.J.); qyucacc@126.com (Q.Y.); hqzhangcacc@126.com (H.Z.)

³ Airport Engineering Safety and Long-Term Performance Field Scientific Observation and Research Base of Transportation Industry, Beijing 100029, China

⁴ Beijing Subway Engineering Management Co., Ltd., Beijing 100005, China

* Correspondence: jjluo@bjtu.edu.cn; Tel.: +86-136-1130-3609

Abstract: In this study, a refined three-dimensional stratigraphic–structural model is established based on ABAQUS finite element software, and the basis for determining pneumatic and vibration loads is explained in detail. From this, the force characteristics of the segment and bolts with and without a cavity behind the lining under the action of multi-field coupling were analyzed, and the force law and corresponding safety of the segment structure and high-strength bolts were determined. The results show that the peak value of the maximum principal stress on the segment structure caused by the surrounding rock pressure was 92.7 times greater than the variation in the peak value of the maximum principal stress caused by additional loads (pneumatic and vibration loads). Despite this, the safety factor of the segment structure satisfied the code requirements. Compared to the situation with no cavity behind the lining, when the cavity behind the lining was small the stresses of the segment structure were large and concentrated, which increased the possibility of crack development in the segment structure. The nodal stresses and strains on the straight and bending bolts exhibited an approximately “W”-shaped distribution with a cavity behind the lining. In addition to the effect of the preload near the nut, the stress and strain at the central measurement point of the bolt rod at the joint face were larger owing to the coupling effect of multiple fields. The high-strength bolt remained in an elastic state and did not yield with damage.

Keywords: aerodynamic load; vibration load; segment structure; high-strength bolt; force characteristics; structural safety



Citation: Li, F.; Jiang, C.; Cai, G.; Luo, J.; Yu, Q.; Zhang, H.; Wang, L. Study on Force Characteristics and Safety of Segment Structure and Bolts with and without Cavity behind Lining with Multi-Field Coupling. *Buildings* **2023**, *13*, 2108. <https://doi.org/10.3390/buildings13082108>

Academic Editor: Wusheng Zhao

Received: 21 June 2023

Revised: 2 August 2023

Accepted: 15 August 2023

Published: 20 August 2023



Copyright: © 2023 by the authors. Licensee MDPI, Basel, Switzerland. This article is an open access article distributed under the terms and conditions of the Creative Commons Attribution (CC BY) license (<https://creativecommons.org/licenses/by/4.0/>).

1. Introduction

With increasing speed, a train generates a large vibration load and transient shock wave when it enters a tunnel; thus, the segment structures and seam bolts must bear the resulting frequent alternating vibration load and transient high shock wave. Because the lining structure and surrounding rock in the tunnel interact as a whole, the surrounding rock is the main source of the load and the main component of the bearing system. When the cavity behind the lining destroys the restraint between the surrounding rock and the lining structure, it can lead to local stress concentration of the lining structure, easily cracking it. According to Song and Zhang, the cavity behind the tunnel lining accounts for up to 11.56% of tunnel defects, and is an important cause of structural cracking [1]. If a cavity appears behind a tunnel segment structure, the safety of the shield segment structures and bolts is affected.

Few researchers have studied the safety of lining structures based on pneumatic loads. On 27 June 1999, an accident occurred in a tunnel in Fukuoka Prefecture on the

Sanyo Shinkansen Line in Japan, in which concrete weighing approximately 200 kg on the side wall hit a train traveling at high speed. According to the investigation by the Japan Railway Institute of General Technology, the primary cause [2] was poor bonding of the old and new concrete due to the tight construction schedule and the alkali–silica reaction of the concrete; the secondary cause [3] was the effect of long-term pneumatic pressure waves on the secondary lining. Liu et al. [4] analyzed the axial force and bending moment of a molded lining caused by surrounding rock pressure and pneumatic pressure based on a two-dimensional load–structure model, concluding that the pneumatic load had less influence on the safety of the lining without considering lining cracks and defects. Other researchers have studied the effects of train vibration loads on tunnel structures. Peng et al. [5] conducted repeated vibration tests based on dynamic load fatigue model tests of a tunnel substructure and compared and analyzed the vertical compressive stresses and bending stresses in different operating conditions. To study the dynamic response characteristics of the shield tunnel structure and the surrounding soil with the vibration load of the train, Yang et al. [6] used a model test method and concluded that the internal force of the shield tunnel segment structure was mainly concentrated near the supine arch where the vibration load was applied. Ding et al. [7] derived the dynamic response of a tunnel structure to train vibration in different operating conditions based on a stratigraphic–structural model of the surrounding rock and tunnel; the dynamic response of the structure with damage was significantly aggravated when the foundation bottom surface had a cavity. Xu et al. [8] established a finite element model of a circular tunnel and strata to study the damage and dynamic response of a lining structure subjected to long-term train vibration, concluding that the lining damage was located mainly in the supine arch structure. MAM et al. [9] evaluated the cyclic stress–strain and shear strength of untreated and treated marine clay under the effects of wind, earthquake, and traffic loadings. However, the wind load studied at this time is not dynamic. Professor Chengping Zhang’s team at Beijing Jiaotong University has conducted considerable research on the cavity behind the lining. Zhang et al. [10,11] analyzed the cracking pattern of a tunnel lining structure based on the presence of double voids (different sizes and extent) behind the lining under external loads. Based on model tests, Min et al. [12,13] analyzed the fracture rules of lining structures in asymmetric multi-arch tunnels with cavities in the wall and vault under external loads. For the study of shield tunnel segment joints, Jusoh et al. [14] discussed the mechanics response of segmental tunnel lining affected by the segment’s joint and presented a short review of recent research works on joint effects in segment joints in the tunnel lining. However, the effect of train aerodynamic and vibration loads on the lining structure was not considered.

The current structural design of Chinese high-speed railroad tunnels does not consider the impact of pneumatic and vibration loads generated by trains on the segment structure and high-strength bolts, either with or without a cavity behind the tunnel lining. Thus, a systematic in-depth study must be conducted in order to provide a theoretical basis for safe operation of high-speed railroads in China.

The remainder of this paper is organized as follows. Section 2 introduces the material properties, boundary conditions, interactions, determination of aerodynamic and vibration loads, validation method of the 3D finite element calculation model, and details of the calculation process and analysis conditions. Section 3 presents a comprehensive analysis of the dynamic response of the segment structure and bolts with and without a cavity behind the lining, along with the coupling of multiple fields (pneumatic load, vibration load, and surrounding rock pressure) based on the stratigraphic–structural model. In addition, a safety study of the segment structure and high-strength bolts is conducted according to the pertinent codes.

2. Three-Dimensional Finite Element Model and Load Parameter Determination

2.1. Computational Model

The typical dimensions of shield tunnels in China were selected for this study. Figure 1 shows a cross-sectional schematic of a shield tunnel segment structure. The inner and

outer radii of the tunnel are 6.87 m and 7.42 m, respectively; the thickness and width of each ring pipe piece are 0.55 m and 2.0 m, respectively; and the segments are connected by staggered seams. Each segment lining ring consists of eight standard blocks A1–A8 (36°), two neighboring blocks B1–B2 (28.5°), and one capping block k1 (15°). The longitudinal and circumferential joints of the segment lining ring were assembled using 30 mm diameter 8.8 grade high-strength bending bolts and straight bolts, respectively. A preload force of 280 kN was applied to the friction-type bolts; the preload force values were selected from the Code for Structural Steel Design [15] and applied through the load module in the 2020 ABAQUS software.

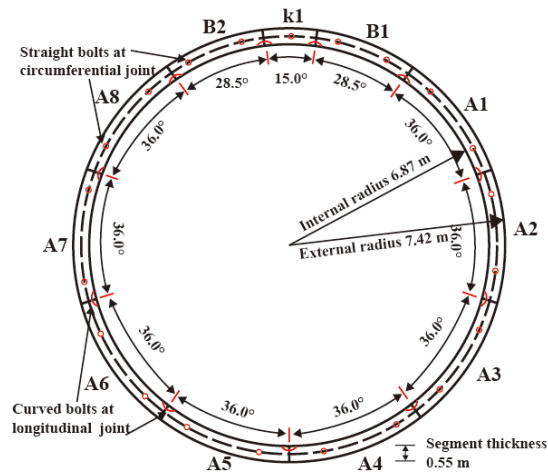


Figure 1. Diagram of cross-section of shield tunnel segment structure.

Figure 2 shows a 3D finite element model of the shield tunnel, including the segment lining rings and joint bolts, three-segment rings with bending bolt connections for the annular pieces, and straight bolt connections for the longitudinal pieces (the direction of train travel). The holes in the high-strength bolts were considered in order to better represent the actual conditions. In the numerical calculations, surface-to-surface contact was used between the segments, between the bolts and the segment, and between the lining rings of the adjacent segments before and after. Hard contact was used in the normal direction and Mohr–Coulomb friction contact was used in the tangential direction; the friction coefficient was taken as 0.6 [16]. Surface-to-surface contact was set up between the lined segment and surrounding rock; the normal direction used a penalty stiffness [17] and the tangential direction used Mohr–Coulomb friction contact with a friction coefficient of 0.8. The segment and elevated arch were considered to be in coordinated deformation, and a tie contact was used.

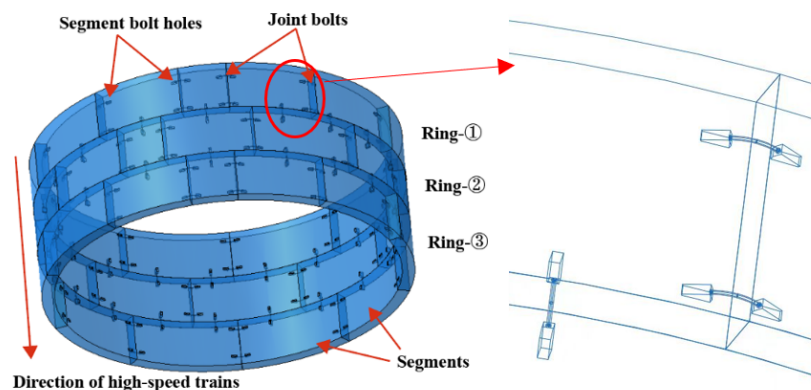


Figure 2. Three-dimensional finite element model of shield tunnel segment structure.

As the model underwent dynamic analysis, the infinite range of the surrounding rock was a key problem in analyzing dynamic interaction. If the selected model range is too large, a significant amount of time is wasted in numerical calculation and storage, and the model may be impossible to complete. At this time, part of the surrounding rock was used for finite domain analysis; thus, it was necessary to set viscoelastic artificial boundary conditions. Liu et al. [18] proposed the concept of artificial boundary conditions and derived an equation for equivalent and consistent viscoelastic boundary conditions that was then verified. The main equations for the equivalent shear model and equivalent elastic model of boundary cells are shown in (1):

$$\begin{cases} \tilde{G} = hK_{BT} = \alpha_T h \frac{G}{R} \\ \tilde{E} = \frac{(1+\tilde{\nu})(1-2\tilde{\nu})}{(1-\tilde{\nu})} hK_{BN} = \alpha_N h \frac{G}{R} \frac{(1+\tilde{\nu})(1-2\tilde{\nu})}{(1-\tilde{\nu})} \end{cases} \quad (1)$$

where \tilde{E} , \tilde{G} , and $\tilde{\nu}$ are the equivalent elastic model, shear model, and Poisson's ratio of the equivalent viscoelastic boundary condition unit, respectively, $\tilde{\nu} = (\alpha - 2)/2(\alpha - 1)$, $\alpha = \alpha_N/\alpha_T$, h is the thickness of the equivalent unit, K_{BT} and K_{BN} are the tangential and normal spring stiffnesses, respectively, α_T and α_N are the tangential and normal viscoelastic artificial boundary parameters, respectively, with α_T generally taking values in the range of 0.35–0.65 and α_N generally taking values in the range of 0.8–1.2, G is the medium shear modulus, and R is the distance from the wave source to the artificial boundary point.

Considering the vibration effect of the train, corresponding damping options should be set when analyzing the dynamic response of the soil and lining structure. The numerical simulation in this study uses Rayleigh damping; two key parameters, the damping ratio and minimum center frequency, must be determined, as shown in Equation (2).

$$\begin{cases} \alpha = \xi_{\min} \omega_{\min} \\ \beta = \xi_{\min} / \omega_{\min} \end{cases} \quad (2)$$

where ξ_{\min} is the critical damping ratio, ω_{\min} is the minimum central frequency, and α and β are constants associated with mass and stiffness, respectively. The formula is $[C] = \alpha[M] + \beta[K]$, where $[C]$, $[M]$, and $[K]$ are the damping matrix, mass matrix, and stiffness matrix, respectively.

According to the monograph by Chen and Xu [19], the critical damping ratio of geotechnical materials generally ranges from 2–5% and the critical damping ratio of structural systems ranges from 2–10%. In this study, the critical damping ratio of the surrounding rock in the numerical calculation was 3% and the damping ratio of the tunnel structure was 5%.

A three-dimensional stratigraphic–structural model was established using ABAQUS software, with a distance of 30 m from the tunnel vault to the ground surface. To reduce the boundary effect, the distance from the constrained boundary to the tunnel center is generally 3–5 times the tunnel span; in this study, the distance from the center of the tunnel to the constrained boundary was four times the tunnel span and the distance from the bottom of the tunnel to the center of the tunnel was three times the tunnel span. The final model size was 120 m × 90 m × 6 m. Figure 3 shows the finite element model of the surrounding rock and lining structure. Figure 3a shows the surrounding rock grid and Figure 3b shows a diagram of the pneumatic and vibration loads applied on the lining wall and rail slab.

To improve calculation efficiency and ensure calculation accuracy, parts of the analysis, such as the segment structure and high-strength bolts, were refined and modeled. The rest of the segment structure was homogenized according to the principle of equivalent flexural stiffness [20], calculated using Equation (3).

$$EI = E_s I_s + E_c I_c \quad (3)$$

where E is the equivalent modulus of elasticity of the segment structure, I is the moment of inertia of the homogeneous model cross-section to the neutral axis, taken as $1.75 \times 10^{-5} \text{ m}^4$ [21], E_s, E_c are the modulus of elasticity of steel reinforcement and concrete, respectively, I_s, I_c are the moments of inertia on the neutral axis of steel reinforcement and concrete, respectively, where $I_s = \pi d^4 / 64$, $I_c = bh^3 / 12$, d is the diameter of steel reinforcement (32 mm), b is the unit length (1000 mm), and h is the segment structure width (550 mm).

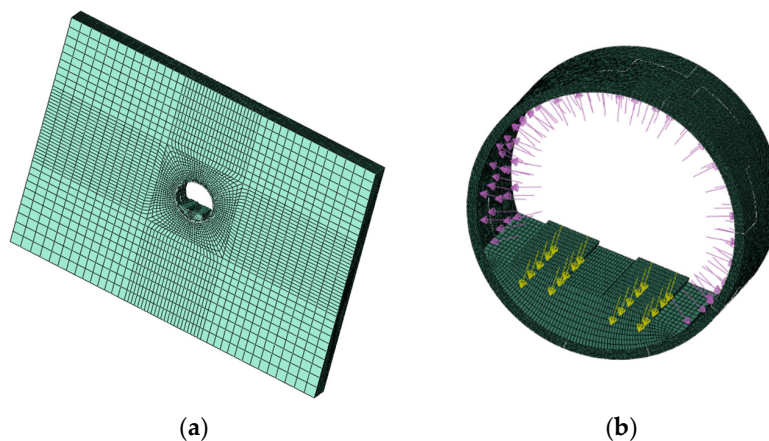


Figure 3. Finite element model of surrounding rock lining structure: (a) surrounding rock grid and (b) diagram of applied pneumatic and vibration loads.

Because the two parameters of the Mohr–Coulomb model are easily obtained and widely used in underground engineering, the surrounding rock in the tunnel was calculated using the Mohr–Coulomb model. According to Pan [22], when a shield tunnel is excavated the ground stress is released, and can be considered at this time by the parametric softening method; the surrounding rock to be excavated is discounted by 30% of the elastic modulus, and the initial stress state of the shield tunnel lining structure during operation can be calculated. At this time, following to the parameter values and reduction coefficients in the literature [22], the surrounding rock parameters used in this paper are shown in Table 1. The lining concrete of the segment was subject to the elastic–plastic damage CDP model established from the literature [23,24]. The joint bolts were modeled as linearly elastic, the concrete grade of the shield tunnel segment was C50, and the inverted arch and rail slab were made of C30 concrete. The relevant parameters for the segment lining, inverted arch, rail slab, and high-strength bolts in Table 1 were obtained according to code [25]. The physical parameters required by the specific model are shown in Table 1.

Table 1. Physical and mechanical parameters of materials.

Materials	Elastic Modulus (GPa)	Poisson Ratio	Friction Angle (°)	Cohesion (kPa)	Density (kN/m ³)	Tensile Strength (MPa)	Compressive Strength (MPa)	Shear Strength (MPa)
Unexcavated surrounding rock	1.5	0.35	28	100	20	/	/	/
Excavated surrounding rock	1.05	0.35	28	100	20	/	/	/
Segment structure	34.5	0.2	/	/	25	1.89	23.1	/
Inverted arch	30	0.2	/	/	24.5	1.43	14.3	/
Rail slab	30	0.2	/	/	24.5	1.43	14.3	/
High-strength bolt	210	0.17	/	/	78.5	400	/	250

2.2. Determination of Most Unfavorable Pneumatic Load

The aerodynamic pressure wave generated when two trains meet in a tunnel is much larger than that generated when a single train runs through the tunnel. Consider two trains meeting in the middle of a tunnel. When the head of train A enters the tunnel, a

compression wave propagates to the tunnel exit to form an expansion wave. When the rear of train B enters the tunnel, the two are superimposed, resulting in stronger expansion wave action on train B. The compression waves generated by the heads of trains A and B pass through the entire tunnel at the same time. If the tunnel is too long, the compression waves are attenuated in the tunnel; if the tunnel is too short, the effect of the compression waves is inadequate, and the tunnel length is unfavorable.

Based on this principle, Equation (4) can be obtained as follows. With a train speed of 350 km/h, the most unfavorable tunnel length was calculated to be approximately 700 m; the result from Equation (4) was consistent with the calculation result when using the formula in the railway industry standard of the People’s Republic of China (TB/T 3503.3-2018) [26]. The time–pressure curve of the pneumatic pressure wave at the central measurement point of the shield tunnel at a height of 1.5 m from the track surface at this speed was derived using a slip grid and Fluent software, as shown in Figure 4. The details of the boundary condition settings and model validation for calculation of the aerodynamic loads are provided in the literature [27–30].

$$\left. \begin{array}{l} L_t/c = L_h/v \\ M = v/c \end{array} \right\} \Rightarrow L_t = 1/M \times L_h \quad (4)$$

where L_t is the most unfavorable tunnel length when trains meet in the tunnel at equal speeds, L_h is the length of the high-speed trains (203 m), v is the speed of the trains, and c is the speed of sound (335 m/s).

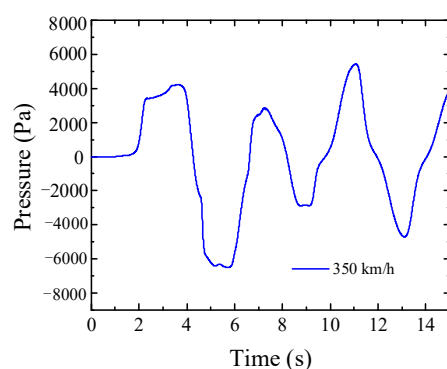


Figure 4. Time–history curve of aerodynamic pressure wave at central measuring point of shield tunnel.

2.3. Determination of Vibration Load and Method Validation

Factors affecting the train vibration load include the train speed, train and rail type, and irregularity, which make it more difficult to determine the train load. High-speed railroad routes are mostly seamless lines with integral roadbeds. The irregularity of the track and the waveform wear effect of the rail surface are the most direct causes of train vibration loads. Most current irregularity management values use British standards [31], as shown in Table 2.

Table 2. UK track geometric irregularity management values.

Control Conditions	L/m	a/m
Based on smoothness of driving	50	16
	20	9
	10	5
Based on additional dynamic loads acting on the line	5	2.5
	2	0.6
	1	0.3
Waveform abrasion	0.5	0.1
	0.05	0.005

At this stage, there are three methods to determine the vibration load of the train, (1) field measurements [32] or inversion of the vibration load of the train based on spectrum analysis [33], although the results obtained using this method are highly discrete; (2) the coupled train–track modeling method, which is too complex in terms of the model and parameters, and insufficiently clear in modeling the wheel–rail contact relationship [34]; or (3) an empirical formula able to accurately represent the vibration load using a simple expression. Liang et al. [31] modified and improved the train load expression proposed by Pan and GN [35] by fully considering the mechanism of vibration load generation (including the train factor, under-rail foundation factor, etc.). The excitation force function they used can better simulate the train vibration load, as shown in Equation (5):

$$P(t) = k_1 k_2 (P_0 + P_1 \sin \omega_1 t + P_2 \sin \omega_2 t + P_3 \sin \omega_3 t) \quad (5)$$

$$P_i = M_0 a_i \omega_i^2 \quad (i = 1, 2, 3) \quad (6)$$

$$\omega_i = 2\pi v / L_i \quad (i = 1, 2, 3) \quad (7)$$

where P_0 is the static load of wheel action, P_1 , P_2 , and P_3 are the corresponding peak power loads, k_1 is the superposition coefficient of adjacent wheel–rail force, k_2 is the rail dispersion coefficient, k_1 is generally taken as 1.2–1.7, and here as 1.6, k_2 is generally taken as 0.6–0.9, and here as 0.8, ω_i is the vibration circle frequency in the unevenness control condition, t is the time, P_i represents the peak power load in the three control conditions, a_i is the typical vector height in mm, L_i is the typical wavelength of the geometrically uneven curve, and v is the train speed.

For the CRH380A high-speed train used in the model, the axle weight was 15 t and the unsprung weight was 750 kg. Considering the operating standards of high-speed railroads, train speeds are increasing; thus, the standards in Table 2 have been adjusted appropriately and correspond to the wavelength and vector height in the three control conditions: $L_1 = 10$ m, $a_1 = 3.5$ mm; $L_2 = 2$ m, $a_2 = 0.4$ mm; $L_3 = 0.5$ m, $a_3 = 0.08$ mm. The time–pressure curve of the vibration load at a train speed of 350 km/h was calculated and is shown in Figure 5.

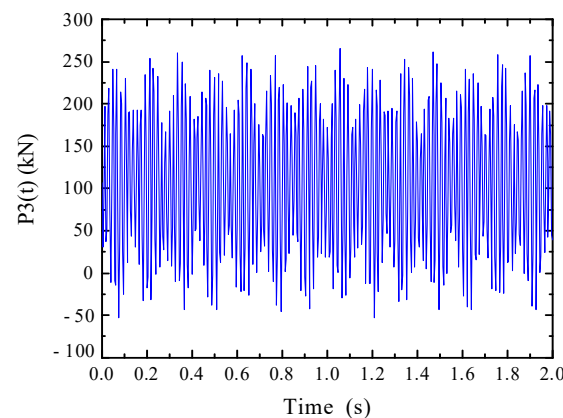


Figure 5. Time–pressure curve of vibration load at train speed of 350 km/h.

To verify the rationality of the determined empirical formula and numerical model, the decay law of the dynamic stress was verified. Because dynamic stresses measured in the field during passage of high-speed trains through a tunnel at speeds above 300 km/h could not be found in the literature, field measurements from sections of the Lanxin–Fuchuan high-speed railway tunnel were used to verify the numerical simulation. The train speed was 150 km/h; the tunnel cross-section of the high-speed railroad and arrangement of the pressure sensors are shown in Figure 6.

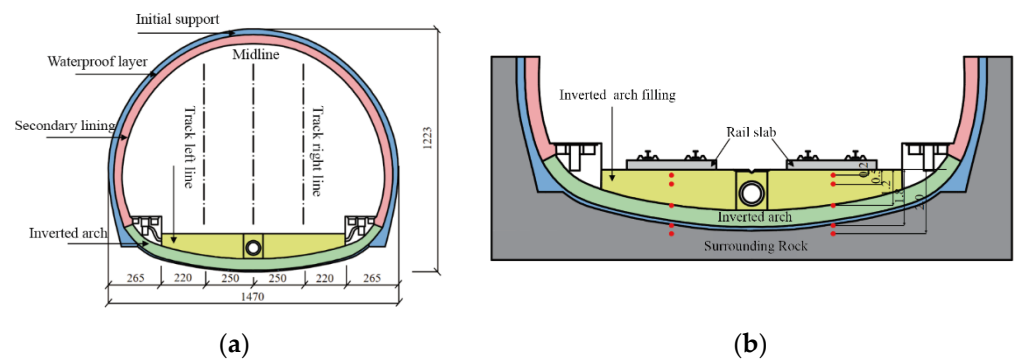


Figure 6. Diagram of tunnel section and pressure sensor arrangement for high-speed railroad: (a) tunnel cross-section and (b) pressure sensor arrangement (unit: cm).

Figure 7 shows the decay curve of the dynamic stress below the track plate with depth at a train speed of 150 km/h. It was found that the field-measured values and the numerical simulation results had the same trend; with increasing depth, the deviations at different positions were 8.2%, 8.1%, 5.1%, and 2.2%. The deviation values were within 10%; thus, the numerical model and empirical formula were considered to be reasonable.

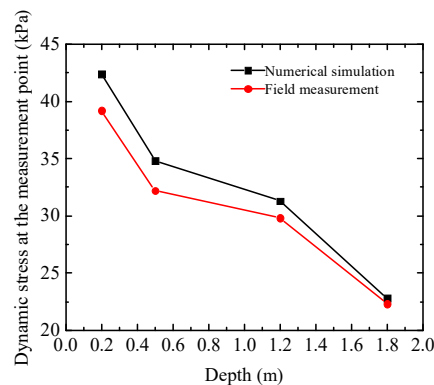


Figure 7. Comparison of numerical simulation and field measurement results.

2.4. Analysis Process and Calculation Conditions

For the dynamic response of the segment structure and bolts with multi-field coupling during passage of a high-speed train through a tunnel, the time period of the aerodynamic load when the head and rear of the train pass through the measurement point was coupled with the vibration load to ensure that the results represent the most unfavorable condition. Using Fluent computational fluid dynamics software and ABAQUS finite element software, the dynamic response and safety of the segment structure and bolts with multi-field coupling were analyzed based on the model CRH380A high-speed train; the specific analysis process is shown in Figure 8.

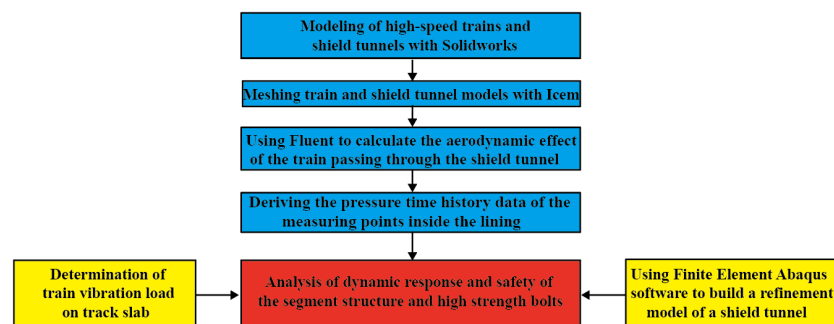


Figure 8. Analysis process.

Solidworks software was used to establish the high-speed train and shield tunnel models (see Figure 9 for details). Icem software was used to mesh the train and shield tunnel models. It should be noted that the bolt holes of the shield tunnel were simplified; see Figure 10 for details. The divided mesh was imported into Fluent, the parameters were set, and the aerodynamic effects on the shield tunnel walls were calculated. The aerodynamic load at the most unfavorable location (the central monitoring point of the shield tunnel) was selected as the basis for analysis, and the train vibration load on the track slab was estimated using empirical formulas (see Formula (5)). With the established 3D finite element model, the calculated pneumatic and vibration loads (see the time–pressure curve in Figures 4 and 5) were imported into ABAQUS in the form of a table in order to analyze the dynamic characteristics and safety of the segment structure and bolts in different working conditions (see Figure 3b for details).

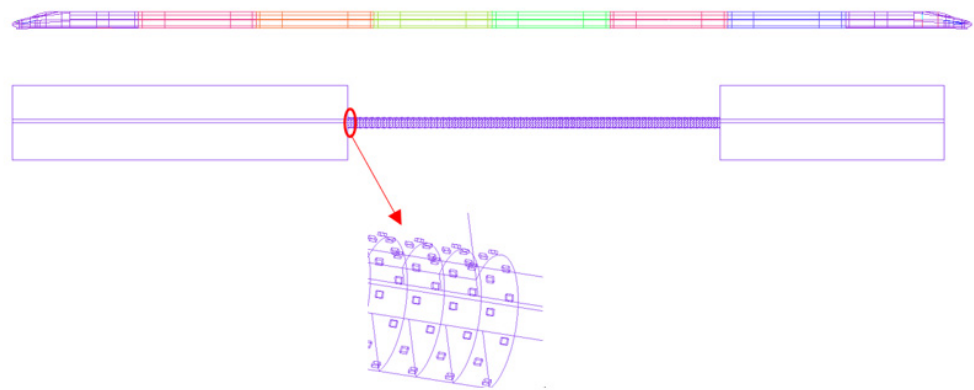


Figure 9. Train and shield tunnel model.

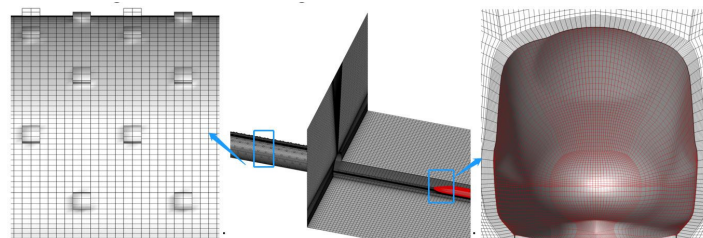
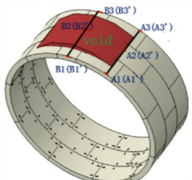


Figure 10. Hexahedral grid for train and shield tunnel.

Table 3 presents the simulated working conditions for the finite element numerical calculations. For convenience of calculation, the effects of the cavity height and cavity length behind the lining were ignored; the cavity height and length in each working condition were defined as 0.5 m and 4.0 m, respectively. For A, with no cavity behind the segment, the debonding behind the vault was analyzed with the midline of the shield tunnel as the symmetry axis. The cavity range was 30° , 45° , and 60° , while the cavity area was symmetrical about the symmetry axis. The schematic diagram of the cavity scheme is provided in Table 3. A1(A1') and A3(A3') are the edge measurement points at the junction position in the cavity and non-cavity areas of the segment, respectively, while A2(A2') is the middle measurement point at the junction in the cavity and non-cavity areas of the segment. The letters outside and inside the brackets indicate the measurement points on the outer and inner sides of the segment, respectively. The same is the case for the other measurement points. For space considerations, only some of the measurement points behind the vault were analyzed.

Table 3. Numerical simulation scheme.

Train Speed (km/h)	Work Conditions	Solutions	Cavity Range			Diagram of the Cavity Range
			Range	Length (m)	Height (m)	
350	No cavity	A D-30°	/	/	/	
	Cavity range behind the vault	D-45°	45°	4	0.5	
		D-60°	60°			

3. Results and Discussion

3.1. Maximum Principal Stress on Segment Structure

3.1.1. Maximum Principal Stress Cloud Map of Segment Structure

The effects of the vibration and pneumatic loads generated by trains passing through the tunnel on the maximum principal stresses in the segment structure were analyzed to determine the extent of the cavity behind the vault. Figure 11 shows the variation in the maximum principal stress clouds in different cavity ranges behind the vault on the outer (Figure 11a–c) and inner (Figure 11d–f) surfaces of the segment structure. The tensile stress is positive, and the compressive stress is negative in the finite element calculation.

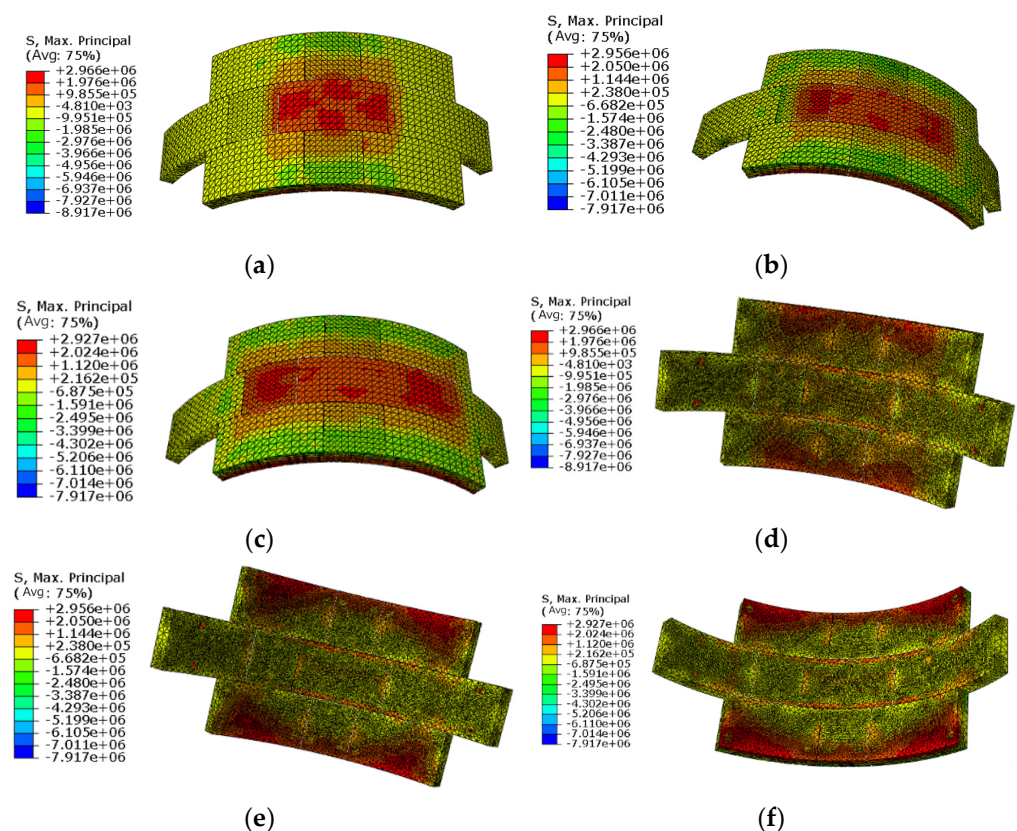


Figure 11. Maximum principal stress cloud maps for segment structures: (a) 30° cavity range behind the vault, outside; (b) 45° cavity range behind the vault, outside; (c) 60° cavity range behind the vault, outside; (d) 30° cavity range behind the vault, inside; (e) 45° cavity range behind the vault, inside; (f) 60° cavity range behind the vault, inside.

From Figure 11, it can be observed that when the cavity behind the lining is small, the stresses on the outside of the vault of the segment structure are concentrated and are the

largest. Tensile stresses appear on the outer surface of the vault of the segment structure, and the range of tensile stresses on the outer surface of the segment structure increases as the cavity range behind the lining increased. Compressive stresses are present around the outer surface of the cavity range. Tensile stresses are formed on both sides of the inner surface of the segment structure, and compressive stresses are formed in the middle. Tensile stress is formed on the outside of the segment within the cavity range and on the inside of the segment at the border of the cavity, while compressive stress is formed elsewhere. The segment structure is prone to cracks at locations with tensile stress and at junctions of tensile and compressive stress.

3.1.2. Variation in Maximum Principal Stresses in Segment Structures with Different Loading Fields

According to the Railway Tunnel Design Code [36], the tunnel lining (segment structure) should be tested for the cross-sectional strength of the members according to the stage of breakage; the ultimate strengths of different concretes are presented in Table 4. The ultimate compressive and tensile strengths of the C50 concrete used in this study are 36.5 MPa and 3.1 MPa, respectively.

Table 4. Ultimate strength of concrete (MPa).

Strength Type	Symbols	Concrete Strength Grade					
		C15	C20	C25	C30	C40	C50
Compressive strength	20	12.0	15.5	19.0	22.5	29.5	36.5
Tensile strength	10	1.4	1.7	2.0	2.2	2.7	3.1

To analyze the effect of the main load (surrounding rock pressure) and additional load (pneumatic and vibration load) on the maximum principal stress on the segment structure with and without a cavity behind the vault, Figure 12 shows the variation in the peak maximum principal stress on the segment structure with different cavity ranges. For convenience, in subsequent analysis “E-S” represents the mechanical response of the segment structure caused by the surrounding rock pressure, “E-S+A-L” represents the mechanical response of the segment structure caused by the surrounding rock pressure and pneumatic load together, and “E-S+A-L+V-L” represents the mechanical response of the segment structure caused by the surrounding rock pressure, pneumatic load of the train, and vibration load together.

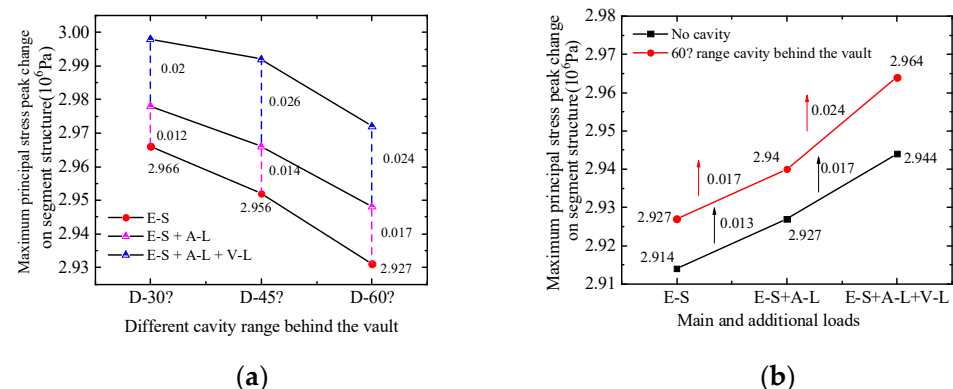


Figure 12. Amplitude change of the maximum principal stress on the lining segment structure of the shield tunnel in different working conditions: (a) different cavity range behind vault and (b) different loading fields.

The maximum principal stress on the segment structure gradually decreases as the size of the cavity behind the vault increases, as shown in Figure 12a, because the stress

concentration is more evident when the cavity range of the vault is small. Overall, the maximum principal stress peak variation in the segment structure due to pneumatic loading is smaller than the maximum principal stress peak variation due to vibration loading, with the former being 60%, 53.8%, and 70.8% of the latter. However, the peak values of the maximum principal stress on the segment structure caused by the surrounding rock pressure are 92.7 times, 74.2, times, and 71.4 times greater than the change in the peak values of the maximum principal stress caused by additional loads (pneumatic and vibratory loads). In Figure 12b, it can be observed that the peak value of the maximum principal stress on the segment structure caused by the surrounding rock pressure is 0.013 MPa greater than that with no cavity. The peak change in the maximum principal stress on the segment structure caused by the pneumatic load is 30.8% greater than that with no cavity, and the peak change in the maximum principal stress on the segment structure caused by the vibration load is 41.2% greater than that with no cavity. This indicates the possibility of structural cracks in the segment structure resulting from the cavity behind the lining.

3.2. Force Characteristics and Safety of Segment Structure

This subsection analyzes the variation in axial force and bending moment on the segment structure with and without a cavity behind the vault through finite element calculations. The stress values on the inner and outer surfaces perpendicular to the most unfavorable condition on the segment structure of the shield tunnel were extracted and the internal force of the section per unit length was calculated based on the stress values on the inner and outer sides of the segment structure. The axial force is the same as described in Section 3.1; the bending moment is positive for inward bending and negative for outward bending. The axial force and bending moment of the segment structure are expressed by Equations (8) and (9) [37]:

$$N = \frac{1}{2}(\sigma_I + \sigma_O)bh \quad (8)$$

$$M = \frac{1}{12}(\sigma_I - \sigma_O)bh^2 \quad (9)$$

where h is the thickness of the segment structure, taken as 550 mm, b is the unit length, taken as 1000 mm, σ_I and σ_O are the inner and outer stress values of the segment structure, respectively, and N and M are the axial force and bending moment of the segment structure, respectively.

After calculation, in order to further analyze the safety of the shield-tunnel lining according to the Railway Tunnel Design Code [32], the tunnel lining was tested for the cross-sectional strength of the elements according to the breakage stage. The safety of the segment structure was determined according to the ratio of the calculated ultimate bearing capacity to the actual axial force and compared with the safety coefficient for concrete structural strength proposed in the code (Table 5). The safety coefficient was calculated using Equation (10):

$$k = N_u / N \geq [k] \quad (10)$$

where k is the safety factor, N_u is the ultimate bearing capacity controlled by the compressive or tensile strength of the member material under axial or eccentric pressure, and $[k]$ is the safety factor required by the code.

Table 5. Strength safety factor of concrete structure.

	Load Combination	Main Load	Main Load + Additional Load
Causes of damage	Concrete reaches compressive ultimate strength	2.4	2.0
	Concrete reaches tensile ultimate strength	3.6	3.0

According to the Railway Tunnel Design Code, when $e_0 \leq 0.2h$ the tunnel lining controls the bearing capacity according to the compressive strength. The compressive strength of the concrete section center and eccentric compressive members are calculated using Equation (11). When $e_0 > 0.2h$, the bearing capacity of the concrete section is determined by the crack resistance requirement, which is calculated from the tensile strength of the material using Equation (12):

$$kN \leq \varphi a R_a b h \quad (11)$$

$$kN \leq \varphi \cdot 1.75 R_1 b h / (6e_0/h - 1) \quad (12)$$

where k is the safety factor, N is the axial force, φ is the longitudinal bending coefficient of the member, with $\varphi = 1.0$ for the tunnel lining, R_a , R_1 are the ultimate compressive and tensile strength of the concrete, respectively, b is the section width, h is the section thickness, e_0 is the section eccentricity distance, and a is the eccentricity influence coefficient of axial force, calculated as $a = 1.0 - 1.5e_0/h$.

The next step is to explore the internal force and safety of the segment structure for different cavity ranges. Figure 13 shows the annular axial force distribution of the segment structure for different cavity ranges behind the vault.

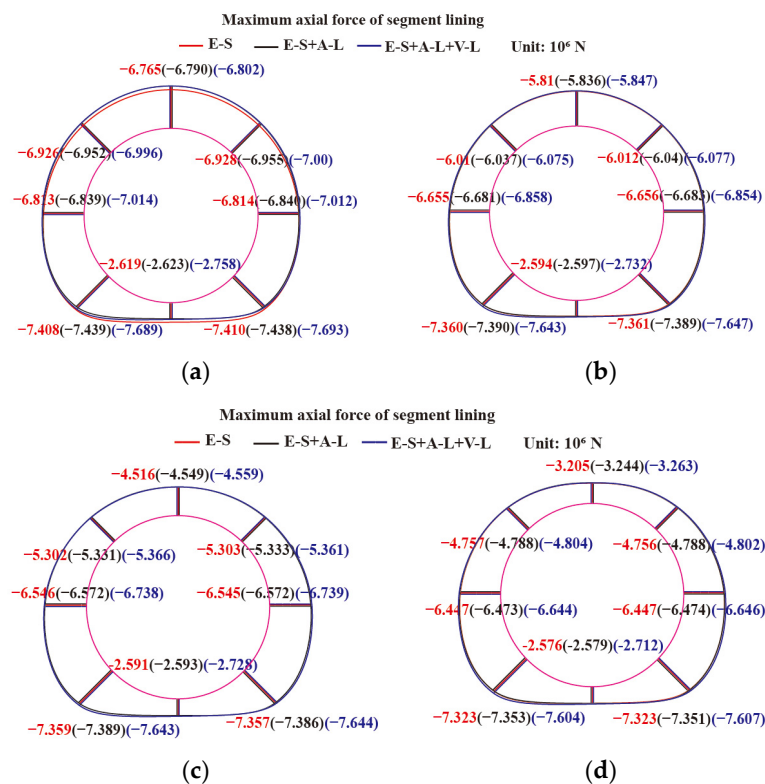


Figure 13. Axial force distribution of segment structure behind the vault with different cavity ranges: (a) no cavity; (b) 30° cavity range; (c) 45° cavity range; (d) 60° cavity range.

As shown in Figure 13, the axial force on the entire segment structure is negative and under pressure, regardless of the presence or absence of a cavity behind the vault. With increasing size of the cavity behind the vault, the axial force at other locations decreases significantly, except for the axial force of the segment structure at the foot and bottom of the arch, which does not change significantly. Figure 13 shows that the axial force at the foot of the arch of the segment structure is the largest and the axial force at the bottom of the arch is the smallest under the pressure of the surrounding rock. Under a pneumatic load, the axial force variation of the segment structure at the bottom of the tunnel is small owing to the influence of the inverted arch and tunnel structure, while the axial force variation at

other locations of the segment structure is more uniform, which is related to the pneumatic pressure applied to the segment structure. Under a vibration load only, the axial force variation in the segment structure at the foot and bottom of the arch is much larger than that at the top and waist of the arch.

Figure 14 shows the distribution of the circumferential bending moment of the segment structure for different ranges of the cavity behind the vault. In Figure 14, the stress concentration in the vault is obvious; the bending moment is the greatest with a 30° cavity range behind the vault. The segment structure at the arch waist changes from a negative outward bending moment to a positive inward bending moment. The influence of the section bending moment is smaller farther from the top of the arch debouching. Figure 14 shows that the bending moment of the segment structure is the greatest at the foot of the arch and during debouching, while the bending moment at the bottom of the arch is the smallest under the pressure of the surrounding rock. Under a pneumatic load, the bending moment of the segment structure at the foot of the arch varies significantly. Only under the action of a vibrational load is the variation in the bending moment of the segment structure at the foot of the arch much larger than the variation in the bending moment at other positions. The dominance of the bending moment on the segment structure caused by the pressure of the surrounding rock indicates that the variation in the bending moment of the segment structure is related to the form of the load, whereas the distribution of the main bending moment diagram is closely related to the structural form of the shield tunnel. From a quantitative perspective, the bending moment of the segment structure with a 30° cavity behind the vault is increased 12.2 times compared to no cavity, while the bending moment of the segment structure at the arch waist is increased by 17.2 times and the bending moment of the foot of the arch far from the vault cavity is increased by 2.1%. This indicates that the bending moment of the segment structure increases for a certain cavity range of the vault, placing great demand on its bending resistance.

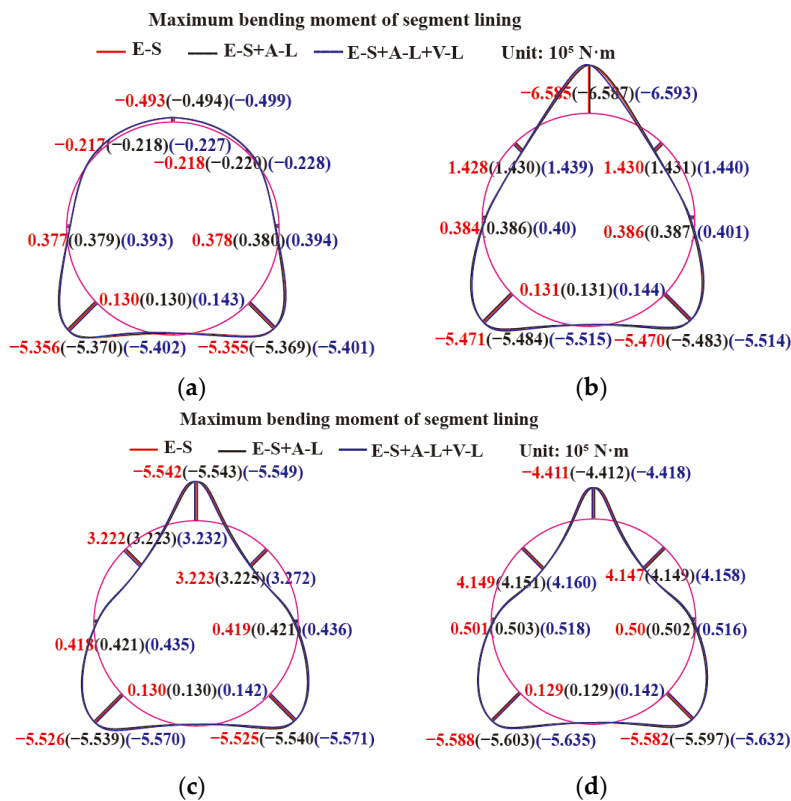


Figure 14. Bending moment distribution of lining section behind the vault with different cavity ranges: (a) no cavity; (b) 30° cavity range; (c) 45° cavity range; (d) 60° cavity range.

Table 6 presents the safety factors of the segment structure for different cavity ranges behind the vault. The axial force values of the segment structure in the shield tunnel in different working conditions under pneumatic load are 0.418%, 0.407%, 0.408%, and 0.41% of the axial force values in the segment structure caused by the surrounding rock pressure. The safety factors of the segment structure reach 647.6, 669.2, 669.2, and 669.2, respectively. With only the train vibration load, the axial force in the segment structure is 3.44%, 3.505%, 3.506%, and 3.496% of the axial force in the tube sheet structure caused by the surrounding rock pressure. The safety factors of the segment structure reach 78.7, 77.8, 77.8, and 78.4, respectively. This indicates that the vibration load has a greater effect on the segment structure at a certain train speed, and that the safety factor of the structure is decreased by more than the effect of the pneumatic load. With only the surrounding rock pressure, the safety factors in the different working conditions decrease to 2.71~2.74, indicating that the surrounding rock pressure is the main factor affecting the safety of the shield tunnel segment structure. Based on the concrete structure safety factor standards in Table 5 and the calculated safety factors in Table 6, it can be concluded that the safety factor of the segment structure meets the specification requirements regardless of the load form and multi-field coupling.

Table 6. Internal force and safety factor of segment structure with different cavity ranges behind the vault.

Working Conditions and Loads		Axial Force (kN)	Bending Moment (kN · m)	Safety Factor	Total Safety Factor
No cavity	Surrounding rock pressure	−7410	−535.6	2.71	2.608
	Negative peak pneumatic pressure (−6.49 kPa)	−31	−3.1	647.6	
	Peak vibration load of the train (266.77 kN)	−255	−4.0	78.7	
30° range cavity behind the vault	Surrounding rock pressure	−7361	−547.1	2.73	2.624
	Negative peak pneumatic pressure (−6.49 kPa)	−30	−3.0	669.2	
	Peak vibration load of the train (266.77 kN)	−258	−4.0	77.8	
45° range cavity behind the vault	Surrounding rock pressure	−7359	−525.6	2.73	2.625
	Negative peak pneumatic pressure (−6.49 kPa)	−30	3.0	669.2	
	Peak vibration load of the train (266.77 kN)	−258	−4.9	77.8	
60° range cavity behind the vault	Surrounding rock pressure	−7323	−588.8	2.74	2.638
	Negative peak pneumatic pressure (−6.49 kPa)	−30	−3.1	669.2	
	Peak vibration load of the train (266.77 kN)	−256	−5.2	78.4	

3.3. Stress–Strain Law of High-Strength Bolts for Segment Structure Connection

Based on the Code for Design of Concrete Structures [25], considering the nonlinear characteristics of the high-strength bolt material, the final elastic–plastic bifold isotropic strengthening model was used for the connection bolt between adjacent segments. The performance grade was 8.8 (yield strength of 640 MPa and tensile strength of 800 MPa) with M30 friction-type high-strength bolt material; the stress–strain relationship of the high-strength bolt is shown in Figure 15. The stress–strain curve in Figure 15 consists of an elastic and a plastic segment. The initial elastic modulus is 210 GPa, the elastic modulus in the strengthening phase is 2.1 GPa, and the Poisson’s ratio is 0.3. When the stress of the high-strength bolt reaches the yield strength, the strain is 0.003 while when the ultimate tensile strength is reached the ultimate tensile strain is 0.08.

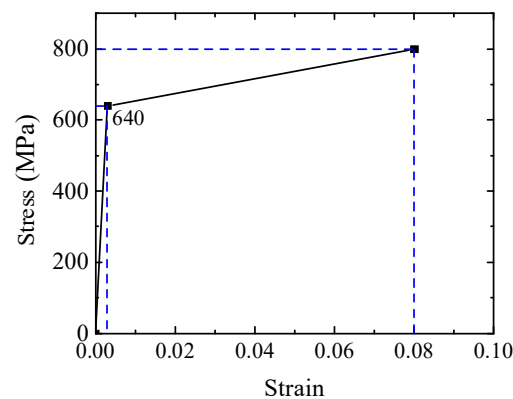


Figure 15. Stress–strain curve of bolt.

The segmented structure of a shield tunnel is typically connected using high-strength bolts. In this study, two types of high-strength bolts, namely, straight bolts and bending bolts, were used for modeling. Because the stresses and strains of the joints differ slightly with different high-strength bolts, the analysis below focuses on the stresses and strains of these high-strength bolt joints and their corresponding safety with high-speed trains passing through shield tunnels with different cavity ranges behind the vault. The von Mises stress is a yield criterion that follows the fourth strength criterion in the mechanics of materials; the material yields when the von Mises stress reaches the yield stress. Thus, von Mises stresses were used in analysis of the high-strength bolts. In order to visually observe changes in the stress and strain in the bolts, the stress and strain clouds of straight and bending bolts in the segment connection with a 30° cavity range behind the vault were analyzed.

Figures 16 and 17 show the stress cloud maps of the straight bolt for a 30° cavity range behind the vault and the variation law of the straight bolt stress along the bolt axis, respectively. The maximum stress of the high-strength bolt reaches 634.2 MPa, while the maximum stress of the bolt rod reaches 155.0 MPa. The bolt rod remains in the elastic stage according to the stress–strain curve for the high-strength bolt. Figures 16 and 17 show that the stress of the bolt rod is greater at the seam surface, while the stress of the high-strength bolt rod far from the seam surface is smaller (with the exception of the nut) and the stress of the bolt near the nut is greater. The overall stress presents an approximately “W”-shaped distribution. The maximum stress of the high-strength straight bolt increases slightly with superposition of the pneumatic and vibration loads of the train. As the stress at the seam surface is easily misaligned under multi-field coupling and the action of mainly vertical pressure, the stresses at the top and bottom of the seam surfaces of the high-strength bolts are relatively large.

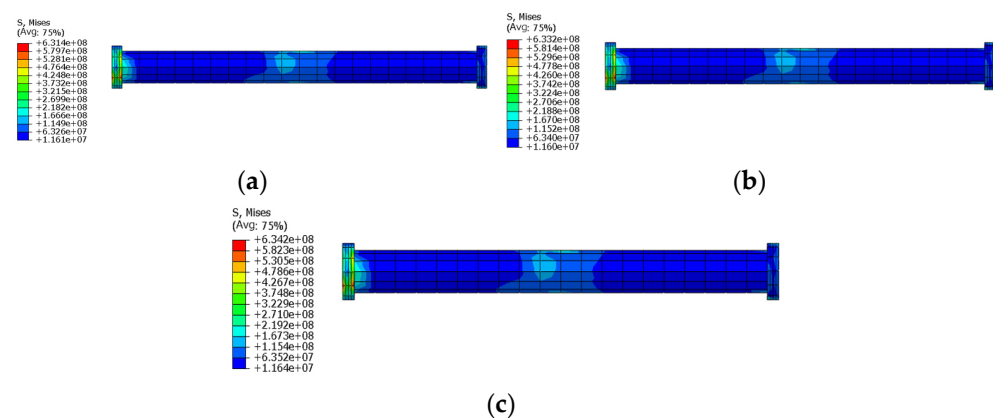


Figure 16. Stress cloud map distribution of straight bolt with a 30° cavity range behind the vault: (a) pressure action of surrounding rock; (b) combined effect of surrounding rock pressure and pneumatic load; (c) combined effect of surrounding rock pressure, pneumatic load, and vibration load.

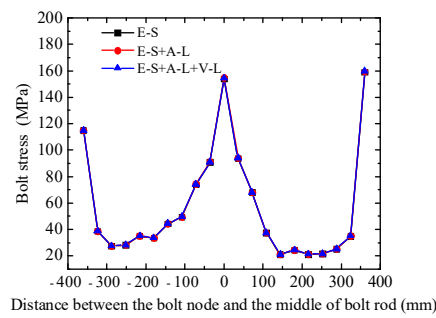


Figure 17. Straight bolt stress along the axis of the bolt with a 30° cavity range behind the vault.

Figures 18 and 19 respectively show the strain cloud maps of the straight bolt with a 30° cavity range behind the vault and the variation law of the bolt strain for the straight bolt along the bolt axis. Based on the stress analysis of the high-strength bolts, it is clear that they remain in the elastic phase. The next analysis considers the maximum principal strain. From Figures 18 and 19, the maximum principal strain of the high-strength straight bolt is 2.973×10^{-3} and the maximum principal strain of the bolt rod is 4.088×10^{-4} . The strain of the high-strength bolt far from the seam surface (except at the nut) tends to be 0, and the strain of the whole bolt presents an approximately “W”-shaped distribution. The maximum principal strain of the high-strength straight bolts increases slightly with superposition of the pneumatic and vibration loads of the train. The strain of the high-strength bolt caused by the pressure of surrounding rock is much larger than the strain caused by pneumatic and vibrational loads. The analysis shows the change laws for the stress and strain of high-strength straight bolts. Next, we consider the change laws for the stress and strain of bending bolts and the difference between bending and straight bolts.

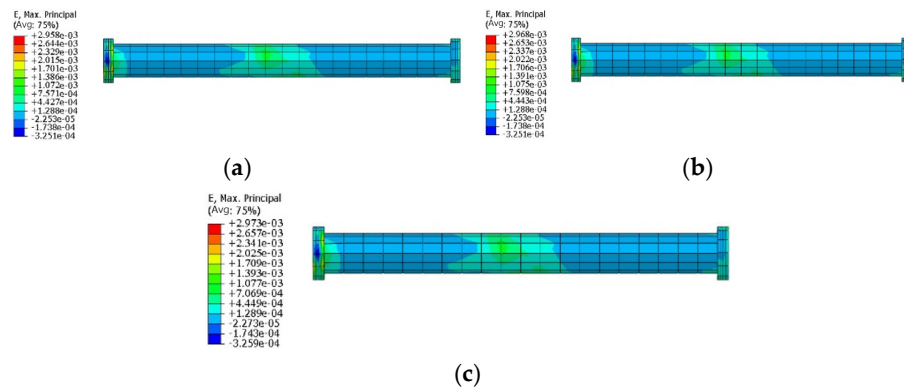


Figure 18. Strain cloud map distribution of straight bolt with a 30° cavity range behind the vault: (a) pressure action of surrounding rock; (b) combined effect of surrounding rock pressure and pneumatic load; (c) combined effect of surrounding rock pressure, pneumatic load, and vibration load.

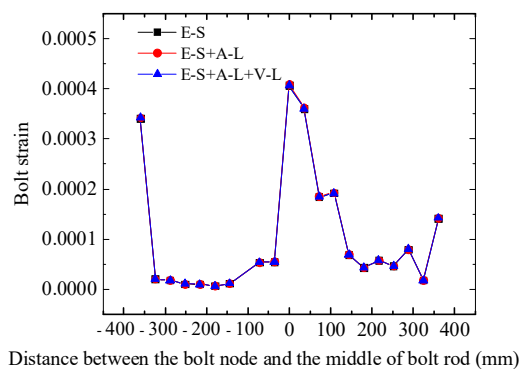


Figure 19. Straight bolt strain along the axis of the bolt with a 30° cavity range behind the vault.

Figures 20 and 21 respectively show the stress cloud maps of the bending bolt with a 30° cavity range behind the vault and the variation law for the bolt stress along the bending bolt axis. The maximum stress of the high-strength bending bolt is 495.5 MPa, the maximum stress of the bolt rod is 102.2 MPa, and the bolt remains in the elastic stage. Compared with the maximum stress of the high-strength straight bolt in the same conditions, the maximum stresses of the bending bolt and bending bolt rod are 78.1% and 65.9%, respectively, of the maximum stress of the straight bolt. The stress in the bending bolt is approximately distributed in a “W” shape about the center of the bending bolt rod.

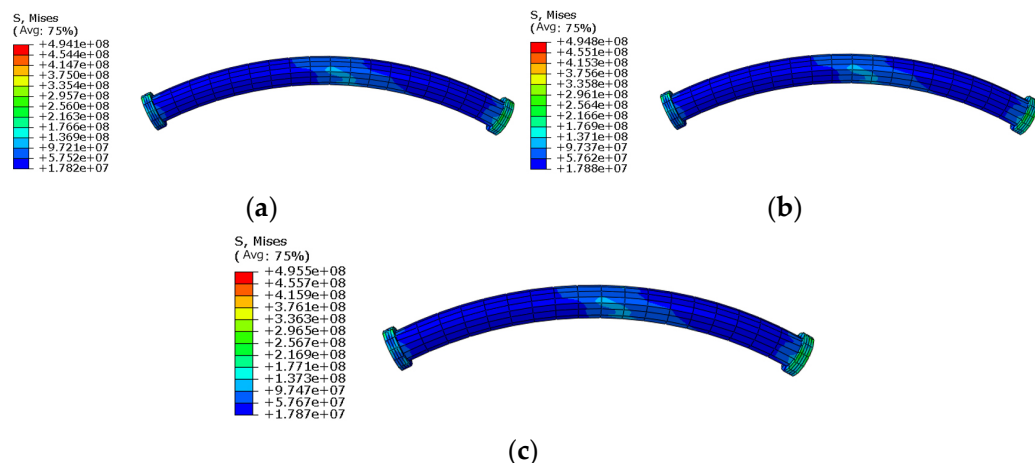


Figure 20. Stress cloud map distribution of bending bolt with a 30° cavity range behind the vault: (a) pressure action of surrounding rock; (b) combined effect of surrounding rock pressure and pneumatic load; (c) combined effect of surrounding rock pressure, pneumatic load, and vibration load.

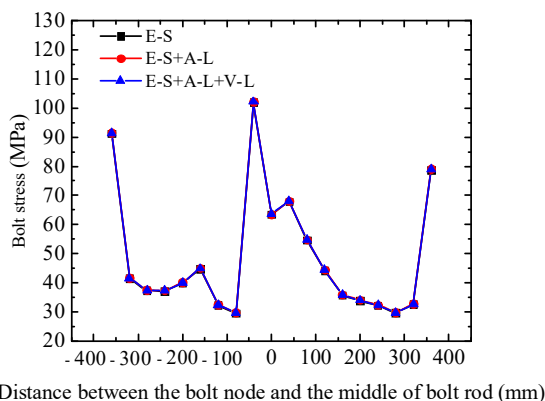


Figure 21. Bending bolt stress along the axis of the bolt with a 30° cavity range behind the vault.

Figures 22 and 23 respectively show the strain cloud maps of the bending bolt with a 30° cavity range behind the vault and the variation law of the bolt strain along the bending bolt axis. The maximum principal strain of the bending bolt is 2.323×10^{-3} and the maximum principal strain of the bending bolt rod is 2.519×10^{-4} . Compared with the strain of the straight bolt in the same conditions, the maximum principal strains of the bending bolt and bending bolt rod are 78.1% and 61.6%, respectively, of the maximum strain of the straight bolt. With superposition of the pneumatic and vibration loads of the train, the maximum principal strain of the bending bolts slightly increases, with the surrounding rock pressure playing a major role.

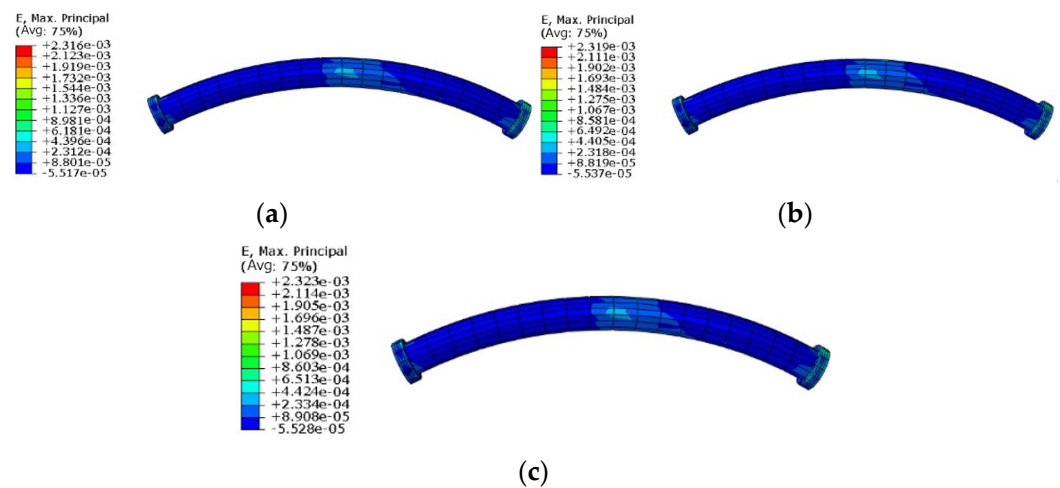


Figure 22. Strain cloud map distribution of bending bolt with a 30° cavity range behind the vault: (a) pressure action of surrounding rock; (b) combined effect of surrounding rock pressure and pneumatic load; (c) combined effect of surrounding rock pressure, pneumatic load, and vibration load.

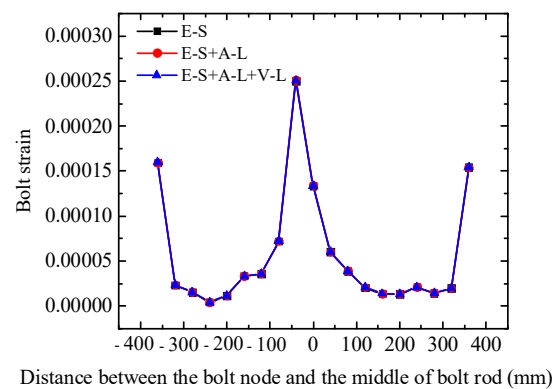


Figure 23. Bending bolt strain along the axis of the bolt with a 30° cavity range behind the vault.

Because the strain of the high-strength bolt is much smaller than the yield strain value and the maximum stress on the bending bolt is smaller than the maximum stress on the straight bolt, the effects of pneumatic and vibrational loads on the stress amplitude were only analyzed for the straight bolt.

Figures 24 and 25 show the variation in the amplitude for high-strength straight bolts due to pneumatic and vibrational loads with different cavity ranges behind the vault. With no cavity behind the lining, the stress on the bolt is relatively small, while the stress amplitude fluctuates with the pneumatic and vibration loads. With a certain cavity range behind the vault, the nodal stress on the high-strength straight bolt caused by the pneumatic and vibrational loads is high in the middle and low on both sides, which is due to the bolt at the seam surface being prone to misalignment with multi-field coupling, causing the stress at this location to be higher than that at other locations in the bolt. Figures 24 and 25 show that as the size of the cavity behind the vault increases, the stress amplitude in the bolts due to vibratory loading is significantly higher than that due to pneumatic loading. The stress on the straight bolts caused by pneumatic loading first increases and then decreases, reaching a maximum stress of 0.31 MPa with a 30° cavity range behind the vault. Both the vibrational load alone and the pneumatic load and vibrational load together produce a gradual increase in the stress in the straight bolts; the maximum stresses are 0.65 MPa and 0.9 MPa, respectively, with a 60° cavity range behind the vault.

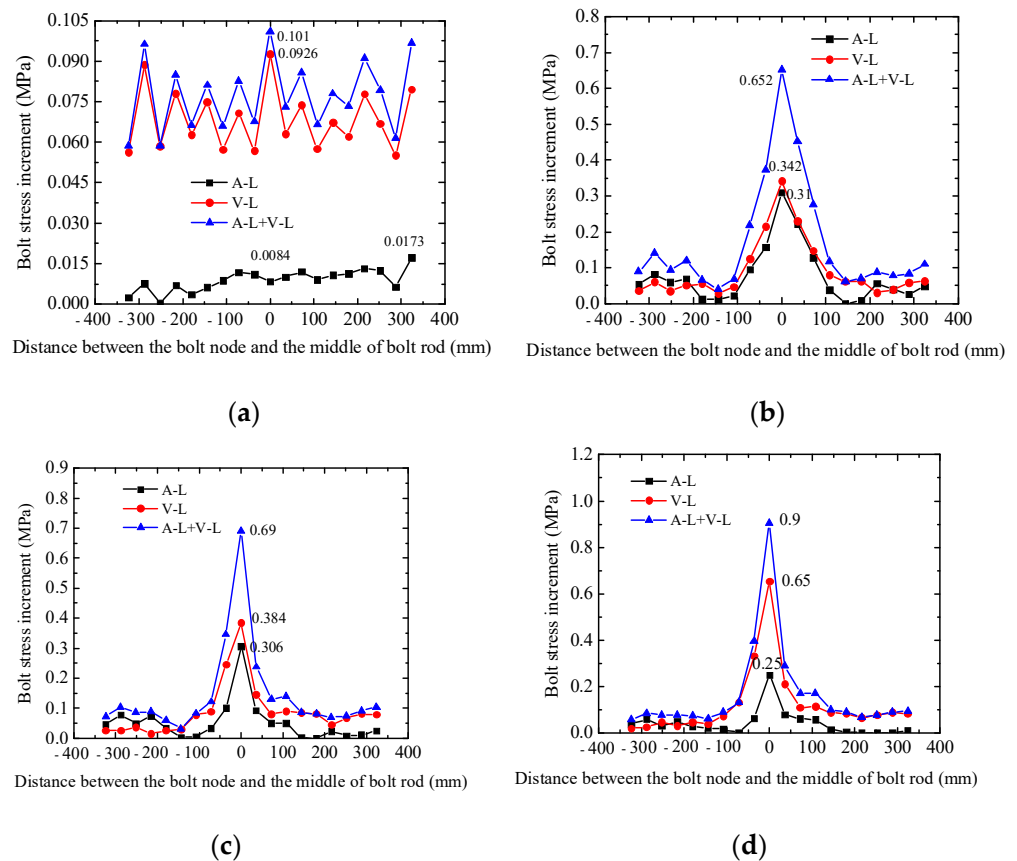


Figure 24. Variation in stress amplitude for straight bolt with different cavity ranges behind vault: (a) no cavity; (b) 30° cavity range; (c) 45° cavity range; (d) 60° cavity range.

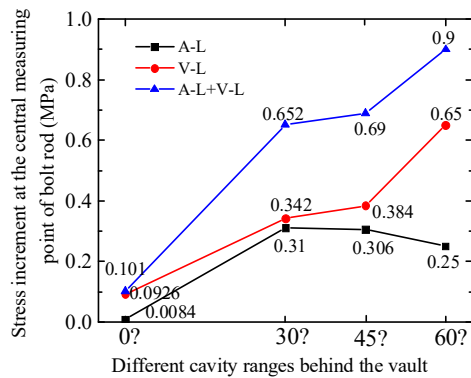


Figure 25. Stress amplitude change at the central measuring point of the straight bolt rod with different cavity ranges behind the vault.

4. Conclusions

A refined three-dimensional stratigraphic–structural model of the surrounding rock was established using finite element software, and the force characteristics of the segment and high-strength bolt were analyzed with and without a cavity behind the vault considering the coupling action of multiple fields in order to determine their safety. The main conclusions of this study are presented below.

(1) The segment structure was under pressure regardless of whether the vault had a cavity behind it. Compared to the situation with no cavity behind the lining, when the cavity behind the lining was small the stresses of the segment structure were large and concentrated, which increased the possibility of crack development in the segment structure. As the cavity range increased, the range of tensile stress on the outside surface

of the segment structure increased. However, as the cavity range increased, the range of tensile stress on the outside surface of the segment structure increased, and the axial force of the segment structure near the cavity was significantly reduced; furthermore, the negative bending moment with a cavity was significantly increased compared with no cavity.

(2) The peak variation in the maximum principal stress caused by the pneumatic load was smaller than the variation in the peak maximum principal stress caused by the vibrational load, with the former being 70.8% of the latter at the maximum. The peak value of the maximum principal stress on the segment structure caused by the surrounding rock pressure was 92.7 times greater than the change in the peak value of the maximum principal stress caused by additional loads (pneumatic and vibrational loads).

(3) With only the pneumatic load, the maximum axial force of the segment structure was 0.418% of the axial force in the segment structure caused by the surrounding rock pressure. With only the train vibrational load, the maximum axial force of the segment structure was 3.506% of the axial force in the segment structure caused by the surrounding rock pressure. This indicates that the pressure of the surrounding rock is the main factor affecting the safety of the shield tunnel segment structure.

(4) With a cavity behind the vault, the nodal stresses and strains on the straight bolts and bending bolts presented an approximate “W” shape. The strains of the bolts were much smaller than the yield strain. The maximum stresses on bending bolts were smaller than the maximum stresses on straight bolts.

(5) With no cavity behind the lining, the stress on the bolts was relatively small, while the stress amplitude fluctuated with the pneumatic and vibration loads. With a certain cavity range behind the vault, the nodal stress on the high-strength straight bolts caused by pneumatic and vibrational loads was high in the middle and low on both sides, as the bolts were prone to misalignment with multi-field coupling at the seam surface, causing the stress at this location to be higher than at other locations in the bolt.

In conclusion, the influence of the aerodynamic load was the lowest, followed by the vibrational load, and the influence of the surrounding rock pressure on the structure was the greatest. Under the action of the surrounding rock pressure, train vibrational load, and pneumatic load, the segment structure and high-strength bolts met the requirements of the specification, and will not sustain damage.

Author Contributions: F.L. collected and analyzed the data and conceived, designed, wrote, and revised the paper; C.J. conceived and designed the analysis, provided the funding, and revised the paper; G.C. provided guidance on numerical simulation software; J.L. provided the train model; Q.Y. wrote, edited, and supervised the paper; H.Z. wrote, edited and supervised the paper; L.W. curated the data and wrote, reviewed, and edited the paper. All authors have read and agreed to the published version of the manuscript.

Funding: This research was funded by the National Natural Science Foundation of China, grant number (51878038). The authors are grateful to all of the study participants.

Acknowledgments: The authors gratefully acknowledge the support of the National Natural Science Foundation of China (grant 51878038). The funders had no role in the experimental design, model establishment, data analysis, manuscript writing, or decision to submit this article for publication. The authors thank the anonymous reviewers who provided valuable suggestions that improved the manuscript.

Conflicts of Interest: The authors declare no conflict of interest.

References

1. Song, R.G.; Zhang, D.L. Analysis on cause of fracturing failure of tunnel lining. *Chin. J. Geol. Hazards Control* **2004**, *15*, 69–72. (In Chinese)
2. Yan, J.X. Japanese railroad tunnel lining has hidden problems. *World Tunn.* **2000**, *1*, 40.
3. Asakura, T.; Kojima, Y. Tunnel maintenance in Japan. *Tunn. Undergr. Space Technol.* **2003**, *18*, 161–169. [[CrossRef](#)]

4. Liu, T.H.; Wang, L.; Li, L.; Yang, F.; Chen, Z.W.; Liu, H.K. Pressure waves acting on wall of a tunnel and their impact on the tunnel's structural safety. *J. Cent. South Univ.* **2021**, *28*, 3223–3237. [[CrossRef](#)]
5. Peng, L.M.; Huang, L.C.; Liu, S.L. Study on dynamic response of railway tunnel bedding structure. *J. Vib. Shock* **2006**, *25*, 175–179.
6. Yang, W.B.; Chen, Z.Q.; Xu, Z.Y.; Yan, Q.X.; He, C.; Wei, K. Dynamic response of shield tunnels and surrounding soil induced by train vibration. *Rock Soil Mech.* **2018**, *39*, 537–545.
7. Ding, Z.D.; Peng, L.M.; Lei, M.F.; Shi, C.H. Analysis of influence factors on dynamic response of high-speed railway tunnel under vibration load. *J. Railw. Sci. Eng.* **2011**, *8*, 1–6.
8. Xu, L.H.; Ma, M.; Liu, W.N. Distribution and evolution characteristics of circular tunnel lining damage due to long-term train loads. *Eng. Mech.* **2020**, *9*, 144–152.
9. Al-Bared, M.A.; Harahap, I.S.; Marto, A.; Mohamad, H.; Alavi Nezhad Khalil Abad, S.V.; Mustafa, Z. Cyclic behavior of RT-cement treated marine clay subjected to low and high loading frequencies. *Geomech. Eng.* **2020**, *21*, 433–445.
10. Zhang, C.P.; Feng, G.; Zhang, X.; Han, K.H.; Zhang, D.L. Effect of double voids behind lining on safety state of tunnel structures. *Chin. J. Geotech. Eng.* **2015**, *37*, 487–493.
11. Zhang, X.; Zhang, C.P.; Feng, G.; Han, K.H. Experimental studies on effect of voids behind tunnel linings on progressive failure process of tunnel structures. *Chin. J. Geotech. Eng.* **2017**, *39*, 1137–1144.
12. Min, B.; Zhang, X.; Zhang, C.P.; Gong, Y.P.; Yuan, T.F. Mechanical behavior of double-arch tunnels under the effect of voids on the top of the middle wall. *Symmetry* **2018**, *10*, 703. [[CrossRef](#)]
13. Min, B.; Zhang, C.P.; Zhang, X.; Wang, H.L.; Li, P.F.; Zhang, D.L. Cracking performance of asymmetric double-arch tunnels due to the voids behind linings. *Thin-Walled Struct.* **2020**, *154*, 106856. [[CrossRef](#)]
14. Jusoh, S.N.; Mohamad, H.; Marto, A.; Yunus, N.M.; Kasim, F. Segment's joint in precast tunnel lining design. *J. Teknol.* **2015**, *77*, 91–98. [[CrossRef](#)]
15. People's Republic of China (PRC) Ministry of Housing and Urban-Rural Development. *Standard for Design of Steel Structures*; China Building Industry Press: Beijing, China, 2017.
16. Yan, Q.X.; Xu, Y.J.; Zhang, W.L.; Geng, P.; Yang, W.B. Numerical analysis of the cracking and failure behaviors of segmental lining structure of an underwater shield tunnel subjected to a derailed high-speed train impact. *Tunn. Undergr. Space Technol.* **2018**, *72*, 41–54. [[CrossRef](#)]
17. Zhao, W.S.; He, X.Z.; Chen, W.Z.; Yang, J.P.; Yang, H.; Yuan, J.Q. Method for analyzing seismic response of shield tunnel and its application. *Rock Soil Mech.* **2012**, *33*, 2415–2421.
18. Liu, J.B.; Gu, Y.; Du, Y.X. Consistent viscous-spring artificial boundaries and viscous-spring boundary elements. *Chin. J. Geotech. Eng.* **2006**, *28*, 1070–1075.
19. Chen, Y.M.; Xu, D.P. *FLAC/FLAC3D Foundation and Engineering Example*; China Water & Power Press: Beijing, China, 2009.
20. Meng, Y.; Mao, C.; Wu, S.Q.; Chen, Y.; Li, N.; Zeng, Z.Q. Numerical simulation by simplified equivalent static model of reinforced concrete. *J. Tianjin Inst. Urban Constr.* **2011**, *17*, 21–24.
21. People's Republic of China (PRC) Ministry of Housing and Urban-Rural Development. *Standard for Test Methods of Concrete Physical and Mechanical Properties*; China Building Industry Press: Beijing, China, 2019.
22. Pan, J.L. Numerical study on effects of ground stress release on face stability during tunneling. *China Civ. Eng. J.* **2015**, *48*, 275–278.
23. Lubliner, J.; Oliver, J.; Oller, S.; Onate, E. A plastic-damage model for concrete. *Int. J. Solids Struct.* **1989**, *3*, 299–326. [[CrossRef](#)]
24. Lee, J.; Fenves, G.L. Plastic-Damage Model for Cyclic Loading of Concrete Structures. *J. Eng. Mech.* **1998**, *124*, 892–900. [[CrossRef](#)]
25. People's Republic of China (PRC) Ministry of Housing and Urban-Rural Development. *Code for Design of Concrete Structures*; China Building Industry Press: Beijing, China, 2015.
26. *TB/T 3503.3-2018*; Railway Applications-Aerodynamics-Part 3: Requirements and Test Procedures for Aerodynamics in Tunnels. China Railway Publishing House: Beijing, China, 2018.
27. Li, F.L.; Luo, J.J.; Wang, L.; Guo, D.L.; Gao, L.P. Analysis of aerodynamic effects and load spectrum characteristics in high-speed railway tunnels. *J. Wind Eng. Ind. Aerodyn.* **2021**, *216*, 104729. [[CrossRef](#)]
28. Li, F.L.; Luo, J.J.; Wang, L.; Wang, D.K.; Gao, L.P. Wave effects of high-speed trains passing through different tunnel lining types. *J. Wind Eng. Ind. Aerodyn.* **2022**, *224*, 104971. [[CrossRef](#)]
29. Li, F.L.; Luo, J.J.; Wang, D.K.; Wang, L. Aerodynamic characteristics when trains pass each other in high-speed railway shield tunnel. *Appl. Sci.* **2022**, *12*, 6244. [[CrossRef](#)]
30. Luo, J.J.; Li, Z.R.; Wang, L.; Zhao, D.P.; Wu, Y.F. Aerodynamic effect of cross passages at the entrance section of a high-speed railway tunnel in a region with mountains and canyons. *J. Wind Eng. Ind. Aerodyn.* **2020**, *204*, 104268. [[CrossRef](#)]
31. Liang, B.; Luo, H.; Sun, C.X. Simulated study on vibration load of high speed railway. *J. China Railw. Soc.* **2006**, *28*, 89–94.
32. Zhang, Y.Q.; Wang, X.Y. Study Reality and Prospect on the Environment Effect Due to Metro Train. *J. Northern Jiaotong Univ.* **2003**, *27*, 48–51.
33. Sun, X.J. *Prediction of Environment Vibrations Induced by Metro Trains and Mitigation Measures Analysis*; Beijing Jiaotong University: Beijing, China, 2008.
34. Yang, W.B.; Xu, Z.Y.; Chen, Z.Q.; Li, L.G.; Yan, Q.Q.; He, C. Influence of segment joints on dynamic response of shield tunnel and surrounding soft soil due to train induced vibration. *Chin. J. Rock Mech. Eng.* **2017**, *36*, 1977–1988.
35. Pan, C.S.; Pande, G.N. Preliminary deterministic finite element study on a tunnel driven in loess subjected to train loading. *China Civ. Eng. J.* **1984**, *17*, 19–28.

36. National Railway Administration of the People's Republic of China. *Code for Design of Railway Tunnel*; China Railway Publishing House: Beijing, China, 2016.
37. Min, B. *Study on the Cracking Characteristic of Asymmetric Double-Arch Tunnel Linings and Its Influence on Structural Bearing Capacity*; Beijing Jiaotong University: Beijing, China, 2022.

Disclaimer/Publisher's Note: The statements, opinions and data contained in all publications are solely those of the individual author(s) and contributor(s) and not of MDPI and/or the editor(s). MDPI and/or the editor(s) disclaim responsibility for any injury to people or property resulting from any ideas, methods, instructions or products referred to in the content.